

## On computation for a hydrogen atom in arbitrary magnetic fields using finite volume method

Gyanendra P. Sasmal\*

*Department of Engineering Technology and Mathematics, Miami University, Hamilton, Ohio 45011, USA*

Received 5 April 2014; Accepted (in revised version) 30 May 2014

Published Online 8 August 2014

---

**Abstract.** The Schrödinger equation in a 2D cylindrical coordinate system is numerically solved for the ground state and a few excited states of the hydrogen atom in arbitrary magnetic fields. The second order discretization of the PDEs on finite volumes results in a set of algebraic equations that are solved simultaneously using Gauss-Seidel Algebraic Multi-Grid (AMG) solver. The modified Stodola-Vianello method is implemented using Gram-Schmidt orthogonalization process to extract the first few energy states and their wave functions concurrently. A detailed mesh convergence study suggests that both energies and wave functions correctly approach toward the unknown exact solutions.

**PACS:** 03.65.Ge, 31.15.xf, 32.30.-r, 32.60.+i

**Key words:** Schrödinger equation, hydrogen atom, magnetic field, finite volume method, eigenvalues, eigenvectors

---

## 1 Introduction

The problem of hydrogen atoms in magnetic fields of arbitrary strength is of great relevance in astrophysics, atomic and molecular physics, and certain areas of solid-state physics. The Schrödinger equation for a hydrogen atom in a magnetic field is inseparable and unsolvable analytically due to spherical symmetry of Coulomb potential and cylindrical symmetry of magnetic potential. In the absence of a closed form solution, many numerical methods have been adopted to establish high precision energy spectrum of hydrogen atom over a wide range of magnetic strength. There is not much known about the structure of a hydrogen atom with a magnetic field in terms of wave functions. Most approaches use certain wave function expansions or approximations for estimating energy spectrum. Perturbation theory is well suited for weak-field regime [1,2] while adiabatic

---

\*Corresponding author. *Email address:* sasmalgp@miamioh.edu (G. P. Sasmal)

approximation is for very strong-field regime [3,4]. Rösner *et al.* [5] computed the high precision energy spectrum over a wide range of magnetic fields using Hartee-Fock-like methods [6]. The method seemed to perform poorly in the intermediate field region due to competing Coulomb and magnetic forces. A few successful variational calculations have also been reported in [7,8]. Kravchenko *et al.* [9] has provided some outline of exact solutions to this problem in forms of the power series in the radial variable and through the sine of the polar angle. Different numerical methods for the hydrogen atom in a magnetic field have been reported by many authors [10-16], and high precision energy spectrum of the hydrogen atom has been achieved. However, the literature lacks the detailed structure of hydrogen wave functions for low to very high magnetic fields. It is the purpose of this paper to compute both energies and wave functions that approximate toward the exact solutions through mesh convergence study by directly solving the Schrödinger equation numerically for the first few energy states over a wide range of magnetic fields.

## 2 Finite volume formulation and solution procedure

The time-independent Schrödinger equation in a 2D cylindrical coordinate system ( $\rho$ ,  $z$ ) using atomic units for a hydrogen atom (spin down) with a uniform magnetic field aligned with  $z$ -axis can be written as

$$-\frac{1}{2} \left[ \frac{1}{\rho} \frac{\partial}{\partial \rho} \left( \rho \frac{\partial \psi}{\partial \rho} \right) + \frac{\partial^2 \psi}{\partial z^2} - \frac{m^2}{\rho^2} \psi \right] + \left( \frac{\gamma}{2} (m + 2s_z) + \frac{\gamma^2 \rho^2}{8} - \frac{1}{\sqrt{\rho^2 + z^2}} \right) \psi = E \psi, \quad (1)$$

where  $m$  is the magnetic quantum number and the magnetic field strength is  $\gamma = B/B_0$ , where  $B_0 = 2.3505 \times 10^5$  T. The energy  $E$  is measured in atomic units. The symbol  $s_z$  is the spin  $z$ -projection, i.e.  $s_z = -1/2$  in this analysis. Since we adopt an iterative procedure for the first few modes, let the superscript  $n+1$  stands for current iteration value, superscript  $n$  for previous iteration value, and the subscript  $i$  for the  $i^{th}$  mode. For a given  $m$ , if  $i=1,2,3,\dots,N$  modes, there will be  $N$  partial differential equations to be solved simultaneously. If the potential  $V$  is denoted as

$$V = \left( \frac{m^2}{2\rho^2} + \frac{\gamma}{2} (m-1) + \frac{\gamma^2 \rho^2}{8} - \frac{1}{\sqrt{\rho^2 + z^2}} \right), \quad (2)$$

Eq. (1) can be written as

$$-\frac{1}{2} \left[ \frac{1}{\rho} \frac{\partial}{\partial \rho} \left( \rho \frac{\partial \psi_i^{n+1}}{\partial \rho} \right) + \frac{\partial^2 \psi_i^{n+1}}{\partial z^2} \right] + (V^+ \psi_i^{n+1} + V^- \psi_i^n) + \frac{(\psi_i^{n+1} - \psi_i^n)}{\Delta t} = E_i^n \psi_i^n. \quad (3)$$

To facilitate Gauss-Seidel iteration, the potential  $V$  is split into two parts. If  $V$  is positive, it is associated with the current  $\psi$  value and if it is negative, it is associated with the previous  $\psi$  value, i.e.  $V^+ = 0.5(V + |V|), V^- = 0.5(V - |V|)$ . The pseudo-transient term  $(\psi_i^{n+1} - \psi_i^n) / \Delta t$  is added in Eq. (3) to ensure diagonal dominance of the iterative scheme. The first order accuracy of the pseudo-transient term is acceptable since it has no impact on the final solutions. This pseudo-transient term disappears when the solution is converged. Now, the volume integral of Eq. (3) over an infinitesimal control volume is

$$\int \int \int \left[ \frac{1}{2} \left( \frac{1}{\rho} \frac{\partial}{\partial \rho} \left( \rho \frac{\partial \psi_i^{n+1}}{\partial \rho} \right) + \frac{\partial^2 \psi_i^{n+1}}{\partial z^2} \right) - (V^+ \psi_i^{n+1} + V^- \psi_i^n) - \frac{(\psi_i^{n+1} - \psi_i^n)}{\Delta t} + E_i^n \psi_i^n \right] dv = 0. \tag{4}$$

Eq. (4) can be discretized over the control volume  $\Delta v = \rho_P \Delta \rho \Delta z$  ( $\rho_P$  is the radius defined at the center of the cell P in Fig. 1).

$$\frac{1}{2} \left( \frac{\left( \rho \frac{\partial \psi_i^{n+1}}{\partial \rho} \right)_e - \left( \rho \frac{\partial \psi_i^{n+1}}{\partial \rho} \right)_w}{\rho_P \Delta \rho} \rho_P \Delta \rho \Delta z + \frac{\left( \frac{\partial \psi_i^{n+1}}{\partial z} \right)_n - \left( \frac{\partial \psi_i^{n+1}}{\partial z} \right)_s}{\Delta z} \rho_P \Delta \rho \Delta z \right) - (V_P^+ \psi_{iP}^{n+1} + V_P^- \psi_{iP}^n) \rho_P \Delta \rho \Delta z - \frac{(\psi_{iP}^{n+1} - \psi_{iP}^n)}{\Delta t} \rho_P \Delta \rho \Delta z + E_i^n \psi_{iP}^n \rho_P \Delta \rho \Delta z = 0 \tag{5}$$

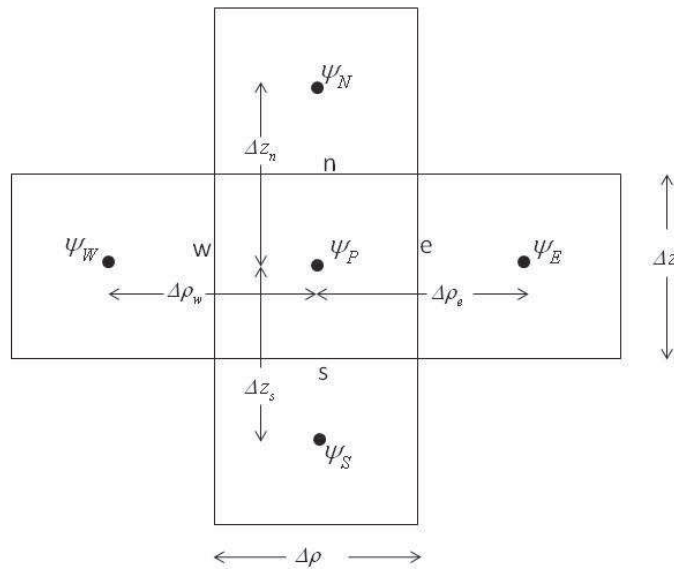


Figure 1: A 2D stencil for finite volume discretization.

The lowercase subscripts  $e, w, n,$  and  $s$  refer to east, west, north, and south faces of the cell  $P$ , respectively as shown in Fig. 1. The uppercase subscripts  $E, W, N,$  and  $S$  are defined at the centers of the east, west, north, and south cells of the cell  $P$ , respectively. Details of finite volume discretization procedures can be found in [17]. Further finite difference approximation of Eq. (5) leads to

$$\begin{aligned} & \rho_e(\psi_{iE}^{n+1} - \psi_{iP}^{n+1}) \frac{\Delta z}{2\Delta\rho_e} - \rho_w(\psi_{iP}^{n+1} - \psi_{iW}^{n+1}) \frac{\Delta z}{2\Delta\rho_w} + (\psi_{iN}^{n+1} - \psi_{iP}^{n+1}) \frac{\rho_P \Delta\rho}{2\Delta z_n} \\ & - (\psi_{iP}^{n+1} - \psi_{iS}^{n+1}) \frac{\rho_P \Delta\rho}{2\Delta z_s} - \left( V_P^+ \psi_{iP}^{n+1} + V_P^- \psi_{iP}^n \right) \rho_P \Delta\rho \Delta z \\ & - \frac{(\psi_{iP}^{n+1} - \psi_{iP}^n)}{\Delta t} \rho_P \Delta\rho \Delta z + E_i^n \psi_{iP}^n \rho_P \Delta\rho \Delta z = 0. \end{aligned} \quad (6)$$

The above equation can be written in a compact form as

$$a_P \psi_{iP}^{n+1} = a_E \psi_{iE}^{n+1} + a_W \psi_{iW}^{n+1} + a_N \psi_{iN}^{n+1} + a_S \psi_{iS}^{n+1} + b_{iP}, \quad (7)$$

where the coefficients are

$$\begin{aligned} a_E &= \frac{\rho_e \Delta z}{2\Delta\rho_e}, \quad a_W = \frac{\rho_w \Delta z}{2\Delta\rho_w}, \quad a_N = \frac{\rho_P \Delta\rho}{2\Delta z_n}, \quad a_S = \frac{\rho_P \Delta\rho}{2\Delta z_s}, \\ a_P &= a_E + a_W + a_N + a_S + \left( \frac{1}{\Delta t} + V_P^+ \right) \rho_P \Delta\rho \Delta z, \\ b_{iP} &= \left( E_i^n - V_P^- + \frac{1}{\Delta t} \right) \psi_{iP}^n \rho_P \Delta\rho \Delta z. \end{aligned} \quad (8)$$

The sufficient conditions for Gauss-Seidel iteration [18] to converge require that  $|a_P| \geq |a_E| + |a_W| + |a_N| + |a_S|$  and for at least one cell  $|a_P| > |a_E| + |a_W| + |a_N| + |a_S|$ . The pseudo-transient term  $1/\Delta t$  and the positive potential  $V^+$  keep the iterative scheme diagonally dominant to ensure convergence. The present discretization is second-order accurate in space. The nucleus is at  $\rho, z = 0$  and the computational domain is  $0 \leq \rho \leq \rho_c$  and  $-z_c \leq z \leq z_c$  where  $\rho_c$  and  $z_c$  are cut-off radial and axial lengths, respectively. The boundary conditions of the current problem are imposed as shown in Fig. 2.

$$\psi = 0 \quad \text{at} \quad \rho = \rho_c \quad \text{and} \quad z = \pm z_c \quad (9)$$

$$\psi \text{ is finite at } \rho = 0. \quad (10)$$

The finite volume formulation has precisely the property of eliminating geometric line singularity (axis of symmetry) and point singularity (nucleus) from the computational domain, satisfying Eq. (10) since the wave function  $\psi$  and the potential  $V$  are volume-averaged and cell-centered. The computational cells adjacent to the axis of symmetry have  $a_W = 0$  in Eq. (8) since  $\rho_w = 0$  at this boundary. Therefore, these cells receive no information from the west side which is 'closed'. This automatically keeps the wave functions finite at the singular line  $\rho = 0$ .

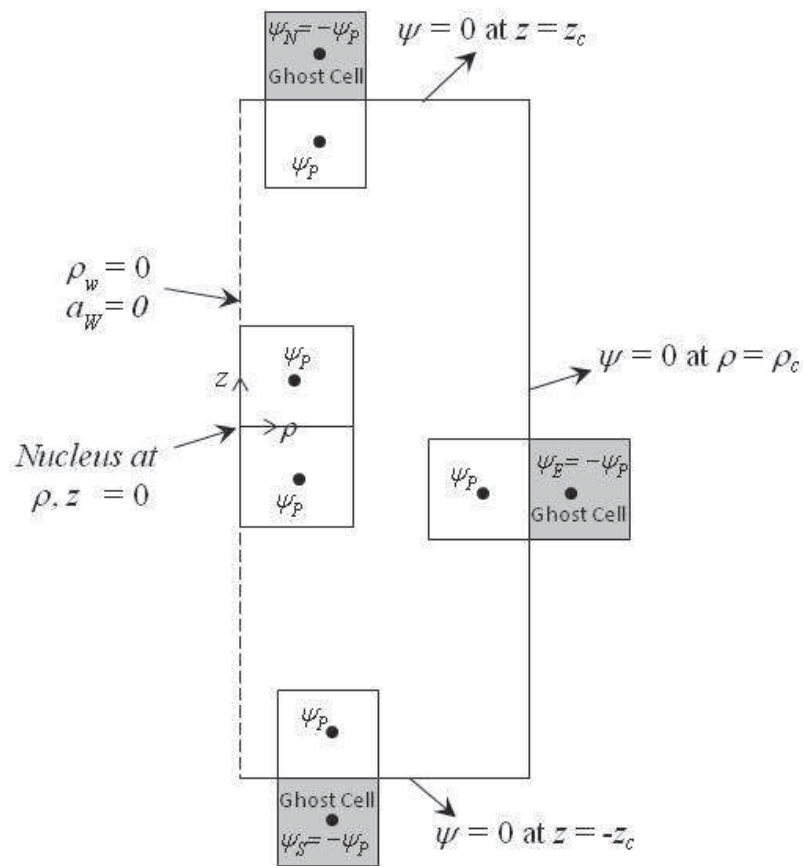


Figure 2: Boundary conditions imposed on the ghost cells.

The present iterative scheme uses a modified Stodolla and Vianello method [19] that converges to the largest negative eigenvalue of the system as the first mode. Hildebrand [20] shows the mathematical proof of this convergence for positive eigenvalue problem in a one-dimensional situation setting the potential  $V=0$ . The higher modes are extracted using the same procedure by removing the lower modes from their computed values after every iteration. These purifications are achieved by Gram-Schmidt orthogonalization process using the "sweeping" technique [21].

The detailed steps of the algorithm are as follows:

*Step 1:* For  $i = 1, 2, 3, \dots, N$  modes, arbitrary initial guesses are made for the wave functions (eigenvectors). They may or may not satisfy the boundary conditions. All the energies (eigenvalues) are set to either a single value or a set of arbitrary values. These initial guesses have superscript  $n$  (previous iteration) in the aforementioned formulation.

*Step 2:* The set of algebraic equations arising from Eq. (7) for all  $N$  modes are solved simultaneously using Gauss-Seidel AMG solver [22]. The new computed values are superscript ' $n+1$ '. The boundary conditions are updated.

*Step 3:* The modified Stodolla Vianello method [19] is used to extract the negative eigenvalues (energies) of the system

$$E_i^{n+1} = \frac{\int \int \int \psi_i^n \frac{\psi_i^{n+1}}{(E_i^n - \beta)} d\nu}{\int \int \int \left( \frac{\psi_i^{n+1}}{(E_i^n - \beta)} \right)^2 d\nu} + \beta = \frac{\sum_{\text{OverAllCells}} \psi_i^n \frac{\psi_i^{n+1}}{(E_i^n - \beta)} \rho \Delta \rho \Delta z}{\sum_{\text{OverAllCells}} \left( \frac{\psi_i^{n+1}}{(E_i^n - \beta)} \right)^2 \rho \Delta \rho \Delta z} + \beta \quad (11)$$

where  $\beta$  is an arbitrary negative constant such that  $|\beta| > |E_1|$  is satisfied, i.e.  $E_1$  is the energy value of the first state. The time step for the problem is set to  $\Delta t = 2/|\beta|$  for numerical stability. For  $\beta = 0$  in Eq. (11), the energy expression leads to positive eigenvalue problems [20].

*Step 4:* The Gram-Schmidt orthogonalization process [21] is used for  $i = 2, 3, 4, \dots, N$  in purifying the higher modes solutions by subtracting out lower mode solutions as follows:

$$\psi_i^{n+1} = \psi_i^{n+1} - \sum_{j=1}^{j=i-1} A_{i,j} \psi_j^{n+1} \quad (12)$$

$$A_{i,j} = \frac{\int \int \int \psi_i^{n+1} \psi_j^{n+1} d\nu}{\int \int \int \left( \psi_j^{n+1} \right)^2 d\nu} = \frac{\sum_{\text{OverAllCells}} \psi_i^{n+1} \psi_j^{n+1} \rho \Delta \rho \Delta z}{\sum_{\text{OverAllCells}} \left( \psi_j^{n+1} \right)^2 \rho \Delta \rho \Delta z} \quad (13)$$

In the above steps, while looping is performed over all the computational cells,  $\psi_i^{n+1}$  gets updated repeatedly. This procedure minimizes the round-off errors and therefore, retains the orthogonality of the wave functions (eigenvectors) more accurately. During the looping process, the wave functions  $\psi_i^{n+1}$  are normalized by their maximum value for each mode to prevent overflow of the numbers for subsequent iteration. The wave function for the first energy state is unaffected in this step, but gets normalized. The boundary conditions are updated again.

*Step 5:* The old value of  $\psi$  is set to  $\psi_i^n = \psi_i^{n+1}$ . Steps 2-5 are repeated until the scaled residual  $R_i$  of Eq. (7) for each mode reaches their absolute minimum value and all the extracted energies do not change anymore up to nine significant digits.

$$R_i = \frac{\sum_{\text{OverAllCells}} \left| a_P \psi_{iP}^{n+1} - a_E \psi_{iE}^{n+1} - a_W \psi_{iW}^{n+1} - a_N \psi_{iN}^{n+1} - a_S \psi_{iS}^{n+1} - b_{iP} \right|}{\sum_{\text{OverAllCells}} \left| a_P \psi_{iP}^{n+1} \right|} \quad (14)$$

### 3 Results

High precision energy spectrums over a wide range of magnetic fields have been well established by many authors. Therefore, they serve as a good benchmark to validate the

Table 1: Different mesh sizes and domains used in the analysis for various  $\gamma$ .

Mesh sizes	Cut-off Boundaries		$\gamma$	Smallest cell size near $\rho=0, z=0$ ( $\Delta\rho, \Delta z$ )
	$\rho_c$	$z_c$		
100 × 200	25	±25	0, 0.02	0.063 698 , 0.063 698
200 × 400	25	±25	0, 0.02, 0.2, 2	0.031 915 , 0.031 915
400 × 800	25	±25	0, 0.02, 0.2, 2	0.015 974 , 0.015 974
600 × 1200	25	±25	0.2, 2	0.010 652 , 0.010 652
200 × 1000	4	±20	20	0.005 106 , 0.010 225
400 × 2000	4	±20	20	0.002 556 , 0.005 115
600 × 3000	4	±20	20	0.001 704 , 0.003 410
100 × 2000	0.8	±20	200	0.002 038 , 0.005 115
200 × 4000	0.8	±20	200	0.001 021 , 0.002 558
300 × 6000	0.8	±20	200	0.000 681 , 0.001 705
100 × 2000	0.5	±20	600	0.001 274 , 0.005 115
200 × 4000	0.5	±20	600	0.000 638 , 0.002 558
300 × 6000	0.5	±20	600	0.000 426 , 0.001 705

current method which is purely numerical. High-precision energy spectrums are difficult to achieve in the present method unless mesh is sufficiently refined. Like other numerical methods, the current method approximates better solutions upon mesh refinement. As reasonable accuracies of energy values are sought, mesh convergence of the wave functions approximating the exact solutions are demonstrated.

Although a general procedure has been presented in Section 2 to solve the hydrogen atom in arbitrary magnetic fields, the present paper only focuses on four states ( $1_{s_0}, 2_{s_0}, 2_{p_0}, 2_{p_{-1}}$ ) to avoid larger computational domain because of increasing cut-off boundary lengths with higher energy states. Therefore, for  $m = 0$ , only three energy states ( $1_{s_0}, 2_{s_0}, 2_{p_0}$ ) are extracted, while for  $m = -1$ , only one energy state ( $2_{p_{-1}}$ ) is extracted. Table 1 shows the mesh sizes, cut-off boundaries, and smallest cell sizes next to the point nucleus for different magnetic strengths. Each case is analyzed using three mesh sizes: a coarse mesh, a finer mesh, and a finest mesh. The computational domain gets narrower (decreasing  $\rho_c$ ) at higher magnetic fields. The cut-off boundaries are carefully selected to ensure that the wave functions asymptotically go towards zero at these cut-off boundaries. As shown in Fig. 3, finer cells are packed near the nucleus and cells get coarser as we move away from the nucleus towards the cut-off boundaries. Fig. 3 is the coarsest mesh in the analysis. Other meshes in Table 1 follow the same trend of packed cells near the nucleus. For all cases, completely arbitrary initial guesses are used for the wave functions and energies at the start (Eq. 15).

$$\begin{cases} \psi_i^n = ie^{-\sqrt{\rho^2+z^2}} \\ E_i^n = i \end{cases} \quad \text{for } m=0 \text{ and } i=1,2,3 \text{ or for } m=-1 \text{ and } i=1. \quad (15)$$

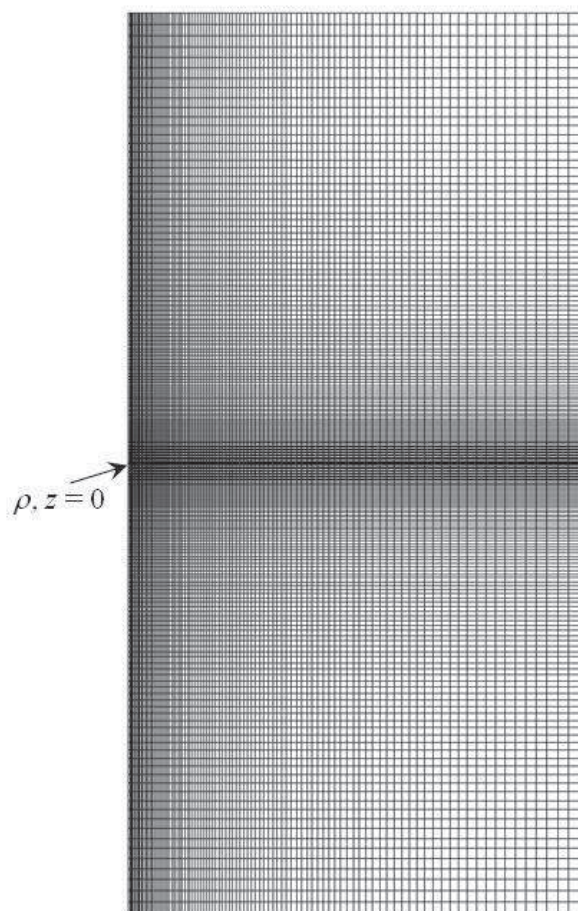


Figure 3: Coarsest mesh ( $100 \times 200$ ) in the analysis.  $0 \leq \rho \leq 25, -25 \leq z \leq 25$ .

For other arbitrary initial guesses, the method converges to the same solutions, confirming the uniqueness of the solutions for a given energy state. The  $\beta$  value in Eq. (11) is set arbitrarily:  $\beta = -2$  for  $\gamma = 0$  to 2,  $\beta = -6$  for  $\gamma = 20$  and 200, and  $\beta = -10$  for  $\gamma = 600$ . This algorithm produces the same solutions for any other  $\beta$  values as long as the condition  $|\beta| > |E_1|$  is satisfied, i.e.  $E_1$  is the energy value of the first state. Using a larger  $\beta$  value can slow down the convergence rate because of the time step constraint  $\Delta t = 2/|\beta|$  [19]. For all cases, the residuals  $R_i$  in Eq. (14) reach their absolute minimum values in the order of  $10^{-12}$  to  $10^{-16}$ .

Table 2 lists the approximate number of AMG iterations for the solutions to converge for all the cases. The  $1s_0$  state converges much faster than  $2s_0$  and  $2p_0$  states. Since  $2p_{-1}$  state is the first energy state extracted for  $m = -1$ , it also converges quickly, like  $1s_0$  state. Cases with magnetic fields,  $\gamma > 600$  were not carried out due to unsuitable aspect ratios of the computational domain and much slower convergence rates for  $2s_0$  and  $2p_0$  states.

Table 2: Approximate number of iterations for the AMG solver to converge.

Mesh sizes	$\gamma$	$1s_0$	$2s_0$	$2p_0$	$2p_{-1}$
$100 \times 200$	0	120	300	300	450
$200 \times 400$	0	120	300	300	450
$400 \times 800$	0	120	450	450	430
$100 \times 200$	0.02	120	300	300	450
$200 \times 400$	0.02	120	300	300	420
$400 \times 800$	0.02	120	300	300	420
$200 \times 400$	0.2	120	1100	1100	200
$400 \times 800$	0.2	120	1100	1100	220
$600 \times 1200$	0.2	200	1100	1100	250
$200 \times 400$	2	120	650	500	120
$400 \times 800$	2	120	800	650	140
$600 \times 1200$	2	150	950	700	200
$200 \times 1000$	20	250	2600	2100	300
$400 \times 2000$	20	500	4500	3600	420
$600 \times 3000$	20	550	6500	4800	580
$100 \times 2000$	200	1600	12000	12000	850
$200 \times 4000$	200	2800	18500	18500	1200
$300 \times 6000$	200	3700	22500	22500	1500
$100 \times 2000$	600	2000	19000	19000	1300
$200 \times 4000$	600	3300	21500	21500	1800
$300 \times 6000$	600	4100	25000	25000	2250

Table 3 shows the complete list of magnetic fields and their energy estimation for different mesh sizes. Only a handful of magnetic strengths over a wide range were chosen in the analyses for validation purposes. The work by Kravchenko *et al.* [9] is used as reference whose energy and magnetic field values are in the same units as the present work. In the literature, the magnetic field strength is often reported as  $\gamma/2$  and the energy in Rydberg unit, which is twice the atomic unit reported here. In Table 3, as the mesh is refined, energies tend to converge towards the high-precision energy values, giving confidence in the present simulation. The errors in energy values are more prominent at high magnetic fields.

For a given state, wave functions are normalized by their maximum value in the computational domain. If  $x$  is an eigenvector,  $-x$  is also an eigenvector. Therefore, sign reversal for the eigenvectors can occur in this numerical method. Signs of the wave function solutions are reversed wherever necessary to make the comparisons among different cases. To study the mesh sensitivity of the solutions, the wave functions on three different mesh sizes are plotted for two extreme cases,  $\gamma = 0$  and  $\gamma = 600$  as shown in Figs. 4 and 5, respectively. For  $\gamma = 0$  (no magnetic field), results are mesh insensitive and are

Table 3: Computed energies on different mesh sizes for various magnetic fields.

Mesh sizes	$\gamma$	$1s_0$	$2s_0$	$2p_0$	$2p_{-1}$
$100 \times 200$	0	-0.501 875	-0.125 278	-0.125 048	-0.125 024
$200 \times 400$	0	-0.500 588	-0.125 084	-0.125 012	-0.125 006
$400 \times 800$	0	-0.500 177	-0.125 025	-0.125 003	-0.125 002
Exact	0	-0.500 000	-0.125 000	-0.125 000	-0.125 000
$100 \times 200$	0.02	-0.511 776	-0.133 908	-0.134 455	-0.143 843
$200 \times 400$	0.02	-0.510 488	-0.133 711	-0.134 419	-0.143 824
$400 \times 800$	0.02	-0.510 077	-0.133 650	-0.134 410	-0.143 819
Ref. [9]	0.02	-0.509 900 044	-0.133 624 177	-0.134 406 465	-0.143 817 610
$200 \times 400$	0.2	-0.590 991	-0.149 114	-0.185 205	-0.250 556
$400 \times 800$	0.2	-0.590 565	-0.149 024	-0.185 189	-0.250 543
$600 \times 1200$	0.2	-0.590 471	-0.149 005	-0.185 186	-0.250 541
Ref. [9]	0.2	-0.590 381 565	-0.148 986 678	-0.185 184 041	-0.250 539 101
$200 \times 400$	2	-1.023 594	-0.174 236	-0.297 970	-0.599 957
$400 \times 800$	2	-1.022 621	-0.174 022	-0.297 776	-0.599 699
$600 \times 1200$	2	-1.022 411	-0.173 980	-0.297 740	-0.599 651
Ref. [9]	2	-1.022 213 907	-0.173 944 705	-0.297 710 972	-0.599 612 773
$200 \times 1000$	20	-2.216 308	-0.224 648	-0.414 191	-1.466 872
$400 \times 2000$	20	-2.215 638	-0.224 044	-0.413 582	-1.465 850
$600 \times 3000$	20	-2.215 508	-0.223 932	-0.413 468	-1.465 660
Ref. [9]	20	-2.215 398 515	-0.223 842 126	-0.413 377 73	-1.465 508 545
$100 \times 2000$	200	-4.746 760	-0.288 594	-0.496 164	-3.382 774
$200 \times 4000$	200	-4.732 083	-0.273 884	-0.481 449	-3.356 050
$300 \times 6000$	200	-4.729 347	-0.271 154	-0.478 719	-3.351 103
Ref. [9]	200	-4.727 145 110	-0.268 968 2	-0.476 532 0	-3.347 145 23
$100 \times 2000$	600	-6.666 493	-0.351 149	-0.552 469	-4.917 173
$200 \times 4000$	600	-6.620 397	-0.303 636	-0.504 941	-4.832 070
$300 \times 6000$	600	-6.611 822	-0.294 815	-0.496 117	-4.816 306
Ref. [9]	600	-6.604 936 099	-0.287 747 4	-0.489 047 0	-4.803 692 91

in excellent match with the exact solutions. For  $\gamma = 600$ , results on three different mesh sizes are graphically indistinguishable, suggesting that they are true approximation of the exact solutions. For all the cases analyzed in this work, wave functions profiles on three different mesh sizes converge to a unique profile for a given state. Since these solutions are difficult to differentiate graphically on different mesh sizes, results on the finest meshes are presented in the rest of the paper.

Figs. 6-9 show the wave function contour plots for all four states with magnetic field

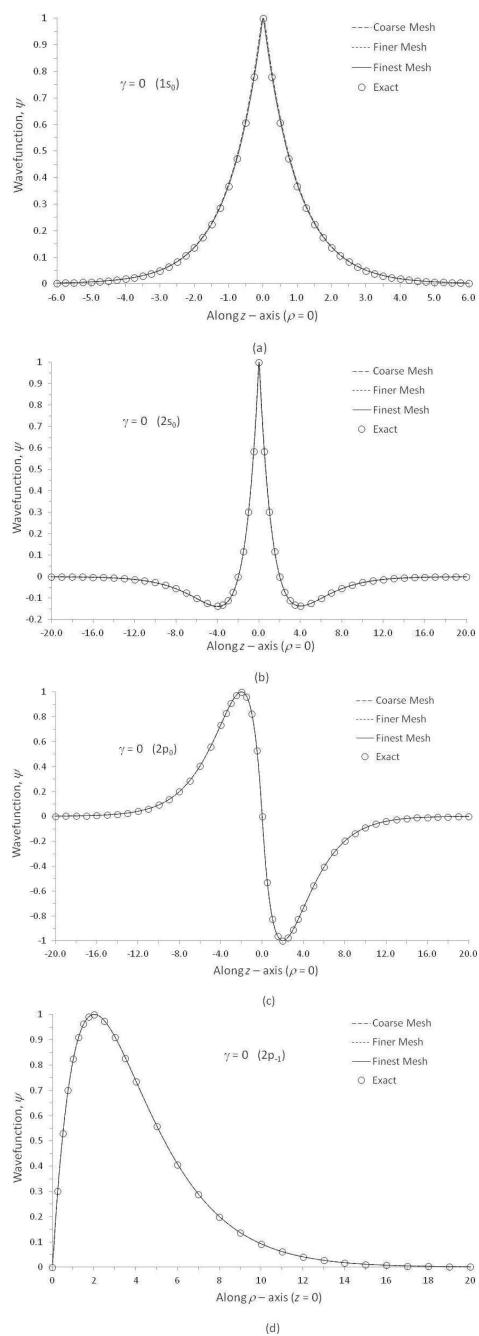


Figure 4: Wave function profiles on three different mesh sizes for  $\gamma = 0$  along  $z$ -axis for (a)  $1s_0$ , (b)  $2s_0$ , (c)  $2p_0$ , and along  $\rho$ -axis for (d)  $2p_{-1}$ .

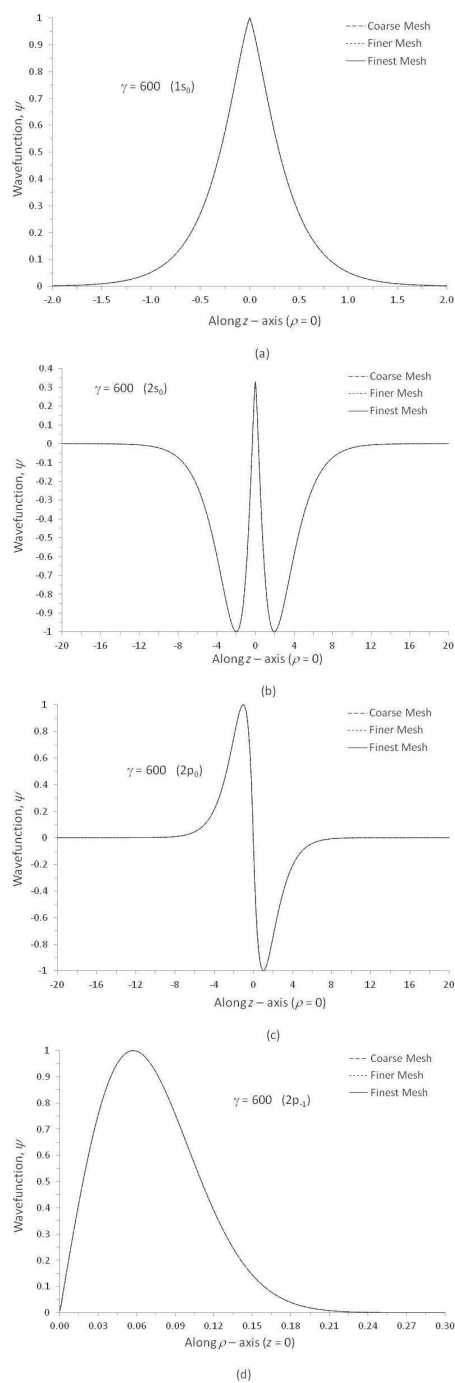


Figure 5: Wave function profiles on three different mesh sizes for  $\gamma = 600$  along  $z$ -axis for (a)  $1s_0$ , (b)  $2s_0$ , (c)  $2p_0$ , and along  $\rho$ -axis for (d)  $2p_{-1}$ .

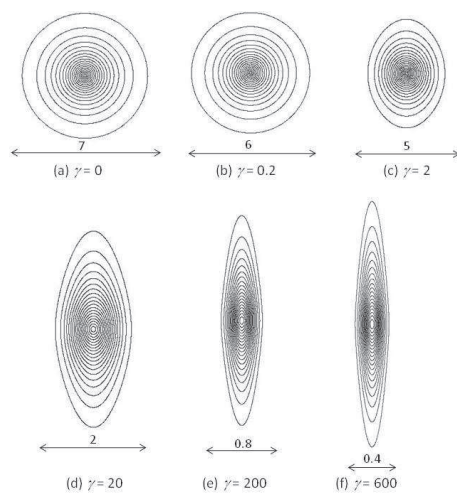


Figure 6: Ground state ( $1s_0$ ) wave function contour plots on the finest meshes for different magnetic fields. Twenty uniform contours between the maximum and minimum values.

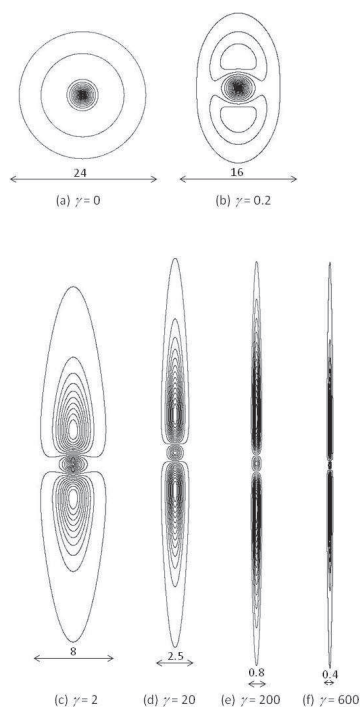


Figure 7:  $2s_0$  wave function contour plots on the finest meshes for different magnetic fields. Twenty uniform contours between the maximum and minimum values.

ranging from  $\gamma = 0$  to 600. The reflection about z-axis is included in these plots for a complete picture. For each plot, a scale is provided showing the dimension of the space

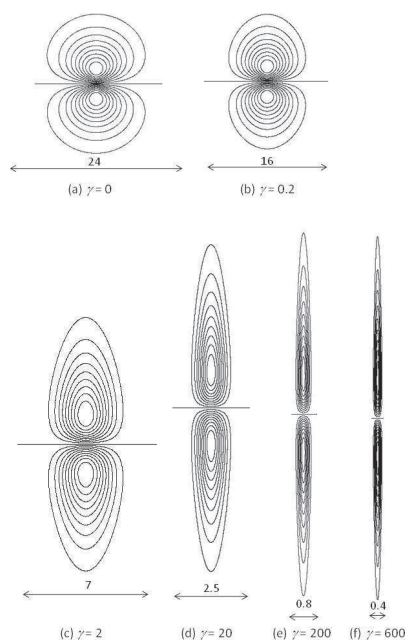


Figure 8:  $2p_0$  wave function contour plots on the finest meshes for different magnetic fields. Twenty uniform contours between the maximum and minimum values.

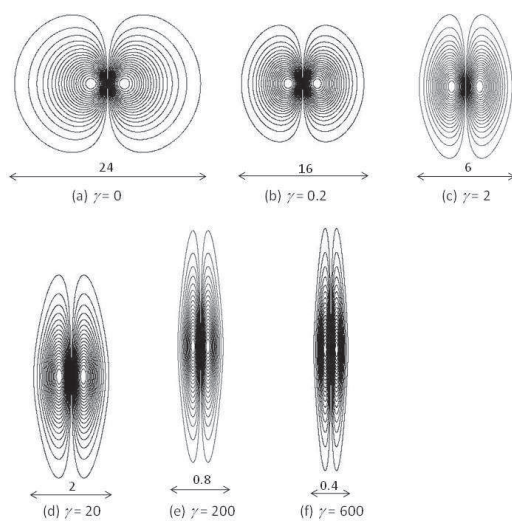


Figure 9:  $2p_{-1}$  wave function contour plots on the finest meshes for different magnetic fields. Twenty uniform contours between the maximum and minimum values.

over which the wave function contours are distributed. With increasing magnetic field, the wave function contours are stretched along the  $z$ -axis with decreasing dimension in space. With increasing magnetic field, the spherical symmetry of the problem is de-

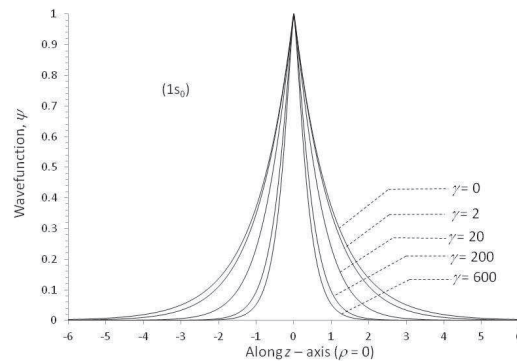


Figure 10: Ground state ( $1s_0$ ) wave function profiles along  $z$ -axis ( $\rho = 0$ ) on the finest meshes for different magnetic fields.

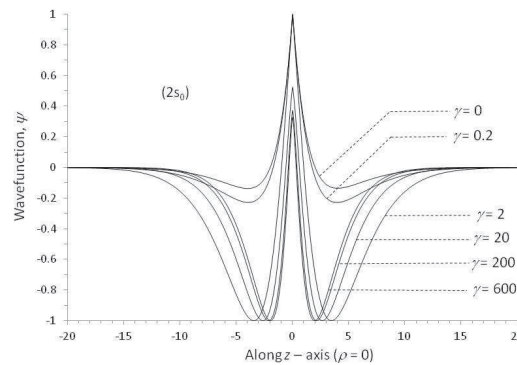


Figure 11:  $2s_0$  wave function profiles along  $z$ -axis ( $\rho = 0$ ) on the finest meshes for different magnetic fields.

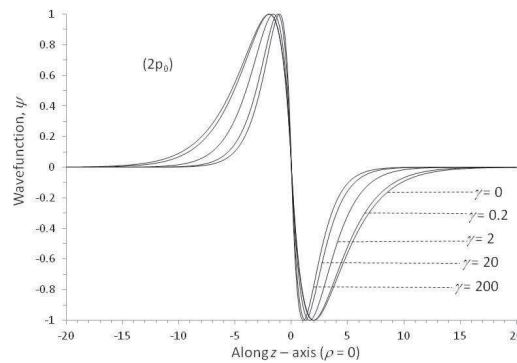


Figure 12:  $2p_0$  wave function profiles along  $z$ -axis ( $\rho = 0$ ) on the finest meshes for different magnetic fields.

stroyed and the cylindrical symmetry of the problem is retained.

For the quantitative comparisons, the wave function profiles for different magnetic fields are plotted for each state as shown in Figs. 10-13. The effects of magnetic fields

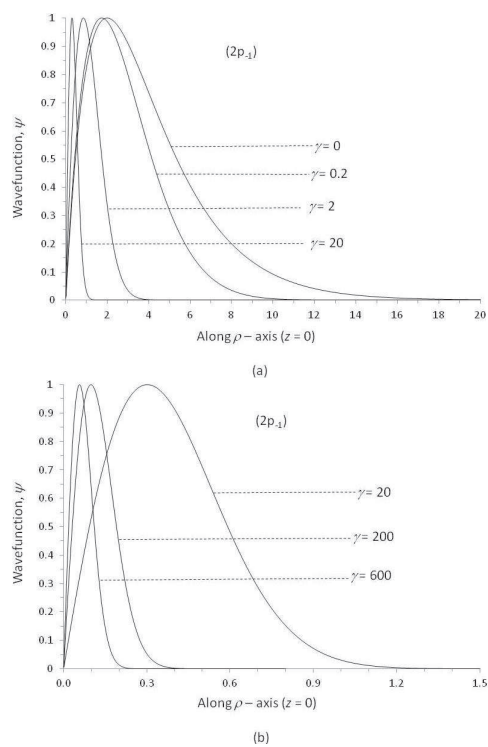


Figure 13:  $2p_{-1}$  wave function profiles along  $\rho$ -axis ( $z = 0$ ) on the finest meshes for different magnetic fields.

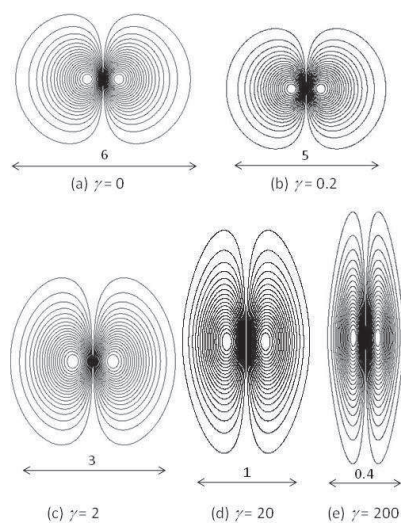


Figure 14: Ground state ( $1s_0$ ) radial probability density in cylindrical coordinate,  $\rho|\psi|^2$  contour plots on the finest meshes for different magnetic fields. Twenty uniform contours between the maximum and minimum values.

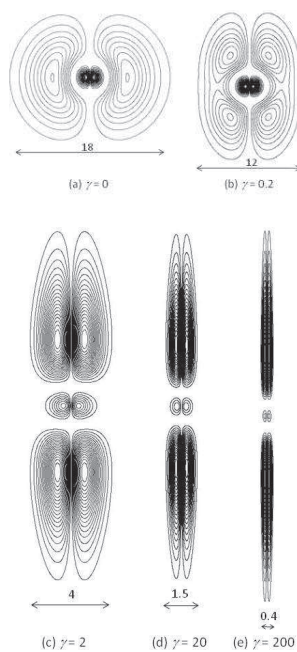


Figure 15:  $2s_0$  radial probability density in cylindrical coordinate,  $\rho|\psi|^2$  contour plots on the finest meshes for different magnetic fields. Twenty uniform contours between the maximum and minimum values.

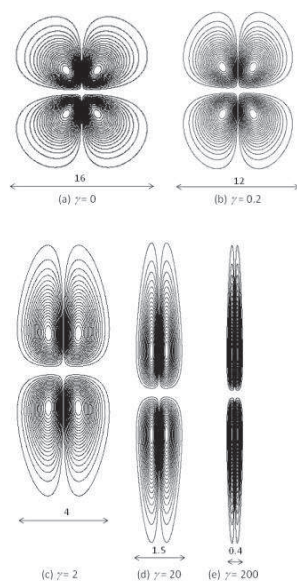


Figure 16:  $2p_0$  radial probability density in cylindrical coordinate,  $\rho|\psi|^2$  contour plots on the finest meshes for different magnetic fields. Twenty uniform contours between the maximum and minimum values.

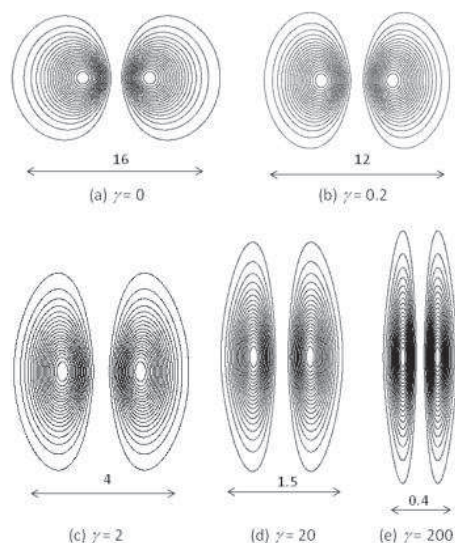


Figure 17:  $2p_{-1}$  radial probability density in cylindrical coordinate,  $\rho|\psi|^2$  contour plots on the finest meshes for different magnetic fields. Twenty uniform contours between the maximum and minimum values.

on the wave functions are quite distinct and intriguing. The competing Coulomb force and magnetic force in the intermediate field region as well as the domination of magnetic force over Coulomb force at higher magnetic fields are quite noticeable in these plots.

For a better interpretation of the wave functions, contours of the radial probability density ( $\rho|\psi|^2$ ) in cylindrical coordinate are shown in Figs. 14-17 with a z-axis reflection for  $\gamma = 0$  to 200. Like wave function contours, the radial probability density contours are stretched along the z-axis with increasing magnetic field as expected.

## 4 Conclusions

A finite volume approach is presented to solve a hydrogen atom in arbitrary magnetic fields. Solutions are smooth, stable, and convergent. The computed wave functions and energies appear to approach toward the exact solutions upon mesh refinement. Wave functions are quantified for the hydrogen atom over a wide range of magnetic fields.

**Acknowledgments.** The author would like to thank the anonymous reviewers for their insightful comments. Computational support provided by Miami University, Oxford campus, Ohio is greatly appreciated.

## References

- [1] R. H. Garstang and S. B. Kemic, *Astrophys. Space Sci.* 31 (1974) 103.
- [2] A. V. Turbiner, *J. Phys. A* 17 (1984) 859.

- [3] R. Cohen, J. Lodenquai, and M. Ruderman, *Phys. Rev. Lett.* 25 (1970) 467.
- [4] C. Liu and A. F. Starace, *Phys. Rev. A* 35 (1987) 647.
- [5] W. Rösner, G. Wunner, H. Herold, and H. Ruder, *J. Phys. B* 17 (1984) 29.
- [6] H. Ruder, G. Wunner, H. Herold, and F. Geyer, *Atoms in Strong Magnetic Fields* (Springer-Verlag, Berlin, 1994).
- [7] J. A. C. Gallas, *J. Phys. B* 18 (1985) 2199.
- [8] S. P. Goldman and Z. Chen, *Phys. Rev. Lett.* 67 (1991) 1403.  
Z. Chen and S. P. Goldman, *Phys. Rev. A* 44 (1991) 4459.  
Z. Chen and S. P. Goldman, *Phys. Rev. A* 45 (1991) 1722.  
Z. Chen and S. P. Goldman, *Phys. Rev. A* 48 (1991) 1107.
- [9] Y. P. Kravchenko, M. A. Liberman, and B. Johansson, *Phys. Rev. A* 54 (1996) 287.
- [10] M. V. Ivanov, *J. Phys. B* 21 (1988) 447.
- [11] J. Shertzer, L. R. Ram-Mohan, and D. Dossa, *Phys. Rev. A* 40 (1989) 4777.
- [12] J. Xi, L. Wu, X. He, and B. Li, *Phys. Rev. A* 46 (1992) 5806.
- [13] V. S. Melezihik, *Phys. Rev. A* 48 (1993) 4528.
- [14] O. L. Filho and A. L. A. Fonseca, *Phys. Rev. A* 50 (1994) 4383.
- [15] P. Fassbinder and W. Schweizer, *Phys. Rev. A* 53 (1996) 2135.
- [16] J. Garcke and M. Griebel, *J. Comp. Phys.* 165 (2000) 694.
- [17] S. V. Patankar, *Numerical Heat Transfer and Fluid Flow* (McGraw-Hill, New York, 1980).
- [18] D. A. Anderson, J. C. Tannehill, and R. H. Pletcher, *Computational Fluid Mechanics and Heat Transfer* (Hemisphere, New York, 1984).
- [19] G. P. Sasmal, *J. Phys. B* 42 (2009) 225001.
- [20] F. B. Hildebrand, *Advanced Calculus for Applications* (Prentice-Hall, New Jersey, 1976).
- [21] C. R. Wylie, Jr., *Advanced Engineering Mathematics* (McGraw-Hill, New York, 1966).
- [22] K. Stueben, *Multigrid*, ed. C. W. Oosterlee, U. Trottenberg, and A. Schuller (Academic, New York, 2001) pp 413-53.